Theoretical investigation of the magnetic and structural transitions of Ni-Co-Mn-Sn metamagnetic shape-memory alloys

Chun-Mei Li,[1,2,*] Qing-Miao Hu,[2] Rui Yang,[2] Börje Johansson,[3,4,5] and Levente Vitos[3,4,6]

[1]*College of Physical Science and Technology, Shenyang Normal University, Shenyang 110034, China*

[2]*Shenyang National Laboratory for Materials Science, Institute of Metal Research, Chinese Academy of Sciences, 72 Wenhua Road, Shenyang 110016, China*

[3]*Applied Materials Physics, Department of Materials Science and Engineering, Royal Institute of Technology, Stockholm SE-100 44, Sweden*

[4]*Condensed Matter Theory Group, Physics Department, Uppsala University, Post Office Box 516, SE-75120 Uppsala, Sweden*

[5]*School of Physics and Optoelectronic Technology and College of Advanced Science and Technology, Dalian University of Technology, Dalian 116024, China*

[6]*Research Institute for Solid State Physics and Optics, Post Office Box 49, Budapest H-1525, Hungary*

(Received 10 December 2013; revised manuscript received 11 June 2015; published 13 July 2015)

The composition-dependent crystal structure, elastic modulus, phase stability, and magnetic property of $Ni_{2-x}Co_xMn_{1.60}Sn_{0.40}$ ($0 \leqslant x \leqslant 0.50$) are studied by using first-principles calculations in combination with atomistic spin dynamics method. It is shown that the present lattice parameters and Curie temperature (T_C) are in agreement with the available experimental data. The martensitic phase transformation (MPT) occurs for $x < 0.43$, where the austenite is in the ferromagnetic (FM) state whereas the martensite is in the antiferromagnetic (AFM) one at 0 K. The x dependence of the lattice parameter, elastic modulus, and energy difference between the FM austenite and the AFM martensite well accounts for the decrease of the MPT temperature (T_M) with the Co addition. With increasing x, the increase of the magnetic excitation energy between the paramagnetic and FM austenite of these alloys is in line with the $T_C \sim x$. The Ni 3*d* as well as the Co 3*d* electronic states near the Fermi level are confirmed mainly dominating the phase stability of the studied alloys.

DOI: 10.1103/PhysRevB.92.024105 PACS number(s): 31.15.A−, 61.66.Dk, 62.20.de, 75.10.−b

I. INTRODUCTION

A new class of metamagnetic shape-memory alloys [1] (e.g., Ni-Co-Mn-In and Ni-Co-Mn-Sn) has attracted much attention in recent years. Due to the magnetic-field-induced martensitic phase transformation (MPT) [1–3], they display high output stress level and relatively large magnetic shape-memory effect (MSME) in comparison with the traditional Ni-Mn-Ga-based alloys [4–6]. Experimentally, a 1.0% one-way and a 0.3% two-way MSME have been observed in $Ni_{1.72}Co_{0.28}Mn_{1.52}Sn_{0.44}$ [7]. The Ni-Co-Mn-Sn group [7–9], containing no expensive element and with considerable MSME, is even more promising for magnetic actuation applications, such as magnetic refrigeration and as a magnetic sensor [10,11].

The magnetic and martensitic transitions of Ni-Co-Mn-Sn are highly composition dependent [12–20]. Different compositions may result in different combination of the Curie temperature (T_C) and the MPT temperature (T_M). Lowering the Sn content relative to that of Mn increases the T_M but decreases the T_C [17,19]. On the other hand, adding more Co content relative to that of Ni increases the magnetization but suppresses the MPT [12,15]. For example, in $Ni_{1.72}Co_{0.28}Mn_{2-x}Sn_x$ [17], with x decreasing from 0.40 to 0.28, T_M goes up from 423 to 561 K whereas T_C goes down from 593 to 393 K. In $Ni_{2-x}Co_xMn_{1.56}Sn_{0.44}$, with x rising up to 0.40, the T_C increases to 450 K [12], while the MPT cannot occur there even in very low temperature because of the decrease of the T_M with increasing x. The different combinations of T_M and T_C result in different properties and also various technological significance of the alloys. In $Ni_{2-x}Co_xMn_{1.60}Sn_{0.40}$ with $x \approx 0.20$ [20], the T_M and T_C are close to each other and consequently the structural and magnetic transitions may couple to each other. This coupling induces some attractive properties such as giant magnetocaloric effect, magnetostriction, and magnetoresistance, which are important for the applications of the magnetic shape memory, energy conversion, or solid-state refrigeration [5,10,21]. To build the connection between the composition and T_M as well as T_C, and to understand their origin and the underlying physics, are critical for designing new Ni-Co-Mn-Sn with desirable properties.

From the atomic scale of investigations, in the present paper we will explore systematically the composition-dependent magnetic and structural transitions of $Ni_{2-x}Co_xMn_{1.60}Sn_{0.40}$ ($0 \leqslant x \leqslant 0.50$). It is known that these studied X_2MnZ types of shape-memory alloys generally possess cubic $L2_1$ structure in the austenite but a tetragonal one in the martensite [22]. Based on first-principles calculations, we first study in detail the composition dependence of the crystal structure, lattice parameters, elastic constants, and free-energy difference between the two phases, and examine their connection with the $T_M \sim x$. Furthermore, in combination with atomistic spin dynamics calculations, the $T_C \sim x$ is estimated, and its correlation with the x dependence of the magnetic excitation energy between the paramagnetic (PM) and ferromagnetic (FM) states of these alloys is investigated. Finally, the electronic origin of the phase stability is presented in combination with the Jahn-Teller theory.

The rest of the paper is arranged as follows: in Sec. II, we describe the first-principles and the atomistic spin dynamics methods we used and the calculation details; in Sec. III, the composition-dependent crystal structure, lattice parameters, elastic constants, phase stability, magnetic property, and

*Corresponding author: cmli@imr.ac.cn

electronic origin are presented. Finally, we summarize the main results of this work in Sec. IV.

II. METHODS AND CALCULATION DETAILS

A. Calculation of the total energy

To carry out the electronic structure and total-energy calculations, the first-principles exact muffin-tin orbitals (EMTO) method [23–27] is used in the present work. Within this program, the Kohn-Sham potential is represented by large overlapping potential spheres, which are optimized by minimizing the deviation between the exact and overlapping potentials. Thus, one describes more accurately the exact crystal potential compared to the conventional muffin-tin or nonoverlapping methods. Another important trait is that the EMTO tool can conveniently incorporate coherent potential approximation (CPA) method [24,27], which is one of the few possible approaches to deal with both the compositional and magnetic disorder at the first-principles level. In a number of previous works, the EMTO-CPA method has been shown to be suitable and accurate enough to compute the anisotropic lattice distortions, and thus the elastic constants of random alloys [23,25,27,28].

For the present application, the exchange-correlation potential is described within the Perdew-Burke-Ernzerhof generalized gradient approximation. The EMTO basis sets include s, p, d, and f components, and the scalar-relativistic and soft-core approximation are employed. The overlapping potential sphere radius (R_{mt}^{Ni}) and the atomic radius ($R_{\mathrm{WS}}^{\mathrm{Ni}}$) on the Ni sublattice are optimized by $R_{mt}^{\mathrm{Ni}} = 0.95R_{\mathrm{WS}}$ and $R_{\mathrm{WS}}^{\mathrm{Ni}} = 1.10R_{\mathrm{WS}}$, respectively, where R_{WS} is the average Wigner-Seitz radius. For the other two sublattices (X=Mn and Sn), the usual setups $R_{mt}^{X} = R_{\mathrm{WS}}$ and $R_{\mathrm{WS}}^{X} = R_{\mathrm{WS}}$ are adopted. The Brillouin zone is sampled by a $13 \times 13 \times 13$ uniform k-point mesh without any smearing technique.

The equilibrium lattice parameters, bulk modulus, and magnetic moments are determined by fitting the total energies versus volume (nine data points) to a Morse function [29]. The elastic constants are calculated with the mathematical formula described in our previous paper [30]. The Debye temperature is obtained by means of the Hill average [31] with Eqs. (6.27) in Ref. [24]. The magnetic ordering is described by three kinds of configurations: (a) the FM state with parallel alignment between Mn on the Mn sublattice (Mn_1) and Mn on the Sn sublattice (Mn_2); (b) the antiferromagnetic (AFM) state with antiparallel alignment between Mn_1 and Mn_2; and (c) the PM state described by the disordered local magnetic model [32]. The number of valence electrons per atom (e/a) is calculated with Ni $3d^8 4s^2$, Co $3d^7 4s^2$, Mn $3d^5 4s^2$, and Sn $4d^{10} 5s^2 p^2$.

B. Calculation of the magnetism

The temperature dependence of the magnetic property is evaluated with the Uppsala Atomistic Spin Dynamics (UppASD) program [33–36]. Within this method, the itinerant electron system is mapped to an effective classical Heisenberg model:

$$H = -\frac{1}{2}\sum_{i \neq j} J_{ij}\mathbf{m}_i \cdot \mathbf{m}_j, \tag{1}$$

where J_{ij} are the interatomic exchange interactions; the indices i and j are 1, 2, and 3, representing the Mn, Ni, and Co atoms. The $\mathbf{m}_i$ is the magnetic moment of atom i, the motion of which is described using the Landau-Lifshitz-Gilbert equation [33,34]:

$$\frac{\partial \mathbf{m}_i}{\partial t} = -\gamma \mathbf{m}_i \times [\mathbf{B}_i + \mathbf{b}_i(t)] - \gamma \frac{\alpha}{m}\mathbf{m}_i\{\mathbf{m}_i \times [\mathbf{B}_i + \mathbf{b}_i(t)]\}. \tag{2}$$

In this expression, $\mathbf{B}_i = -\frac{\partial H}{\partial \mathbf{m}_i}$, is the so-called effective field experienced by each atom i. γ is the gyromagnetic ratio. $\mathbf{b}_i(t)$ is a stochastic magnetic field with a Gaussian distribution with respect to temperature (T), and its magnitude is related to the damping parameter α, which eventually brings the system into thermal equilibrium. With the solved $\mathbf{m}_i$ in the given T, the magnetization (M) and magnetic susceptibility (χ) are then calculated from

$$M = \frac{1}{N}\sqrt{\left(\sum_i m_{x,i}\right)^2 + \left(\sum_i m_{y,i}\right)^2 + \left(\sum_i m_{z,i}\right)^2} \tag{3}$$

and

$$\chi = \frac{1}{k_B T^2}[\langle M^2\rangle - \langle M\rangle^2], \tag{4}$$

respectively, where N(=3) means the three types of magnetic atoms (Mn, Ni, and Co) and k_B is the Boltzmann constant.

In our calculations, the cubic periodic box size is kept to $15 \times 15 \times 15$ unit cells. The time step for solving the above differential equations (2) is 10^{-16} s. The number of the time steps used is 10 000. The α is set at 0.01. Including the interactions between the atoms within the tenth-nearest neighbors, the 0-K J_{ij} are calculated using the magnetic force theorem [37] implemented in the EMTO-CPA program [24].

III. RESULTS AND DISCUSSION

A. Crystal structure

Figure 1 shows the total electronic energies for the FM, AFM, and PM states of $\mathrm{Ni}_{2-x}\mathrm{Co}_x\mathrm{Mn}_{1.60}\mathrm{Sn}_{0.40}$ with $x = 0.10$, as functions of the tetragonal lattice ratio (c/a) and the Wigner-Seitz radius (r_{WS}). For the FM state [Fig. 1(a)], we get only one energy minimum around $R_{\mathrm{WS}} = 2.757$ bohrs and $c/a = 1$, corresponding to the $L2_1$ phase. Nevertheless, for both the AFM and PM states [Figs. 1(b) and 1(c), respectively], the energy shows two minima: one is at $c/a = 1$, meaning the cubic austenite, and another one is around $c/a = 1.20$–1.30, corresponding to the tetragonal martensite. In comparison, in Figs. 1(a)–1(c), the austenite with the lowest energy is in the FM state, whereas the martensite with relative lower energy tends to be in the AFM one. For $\mathrm{Ni}_{1.90}\mathrm{Co}_{0.10}\mathrm{Mn}_{1.60}\mathrm{Sn}_{0.40}$, the electronic energy prefers the austenite in the FM state and the martensite in the AFM one.

The x dependence of the relative electronic energy of the AFM and PM austenite [$\Delta E_{\mathrm{AFM}}^{\mathrm{Aus}}(x)$ and $\Delta E_{\mathrm{PM}}^{\mathrm{Aus}}(x)$] and martensite [$\Delta E_{\mathrm{AFM}}^{\mathrm{Mar}}(x)$ and $\Delta E_{\mathrm{PM}}^{\mathrm{Mar}}(x)$] of $\mathrm{Ni}_{2-x}\mathrm{Co}_x\mathrm{Mn}_{1.60}\mathrm{Sn}_{0.40}$ ($0 \leqslant x \leqslant 0.50$) are listed in Table I. The reference in each x is the electronic energy of the FM austenite [$E_{\mathrm{FM}}^{\mathrm{Aus}}(x)$]. For the austenite, the $\Delta E_{\mathrm{AFM}}^{\mathrm{Aus}}(x)$ is

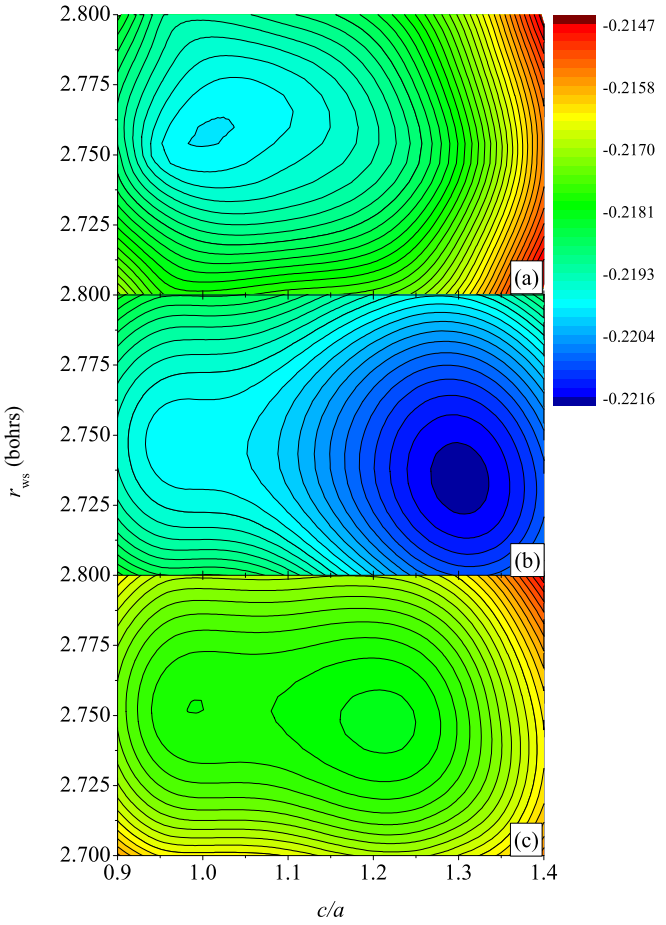

FIG. 1. (Color online) Total electronic energy contours (in Ry) for the (a) FM, (b) AFM, and (c) PM $Ni_{1.90}Co_{0.10}Mn_{1.60}Sn_{0.40}$ alloys as a function of the tetragonal lattice ratio (c/a) and the Wigner-Seitz radius (r_{WS}).

smallest for $x = 0$ whereas for $0.10 \leqslant x \leqslant 0.50$ the FM state tends to be lowest in the energy because of the positive values of both $\Delta E^{Aus}_{AFM}(x)$ and $\Delta E^{Aus}_{PM}(x)$. For the martensite, since $\Delta E^{Mar}_{AFM}(x)$ is always much smaller than $\Delta E^{Mar}_{PM}(x)$ in each x, the AFM state is energetically stabilized for all of these alloys at 0 K.

In Fig. 2, the equilibrium lattice parameters [$a(x)$] of the $L2_1$ phase with FM, AFM, and PM states, respectively, are

TABLE I. Relative electronic energy (in mRy) of the AFM [$\Delta E^{Aus}_{AFM}(x)$] and PM [$\Delta E^{Aus}_{PM}(x)$] austenite and the AFM [$\Delta E^{Mar}_{AFM}(x)$] and PM [$\Delta E^{Mar}_{PM}(x)$] martensite to that of the FM austenite of $Ni_{2-x}Co_xMn_{1.60}Sn_{0.40}$ ($0 \leqslant x \leqslant 0.50$) alloys.

x	$\Delta E^{Aus}_{FM}(x)$	$\Delta E^{Aus}_{AFM}(x)$	$\Delta E^{Aus}_{PM}(x)$	$\Delta E^{Mar}_{AFM}(x)$	$\Delta E^{Mar}_{PM}(x)$
0.00	0.00	−0.28	1.57	−2.16	1.49
0.10	0.00	0.10	1.99	−1.69	1.80
0.20	0.00	0.46	2.40	−1.21	2.08
0.30	0.00	0.82	2.82	−0.71	2.39
0.40	0.00	1.20	3.24	−0.18	2.73
0.50	0.00	1.58	3.65	0.36	3.09

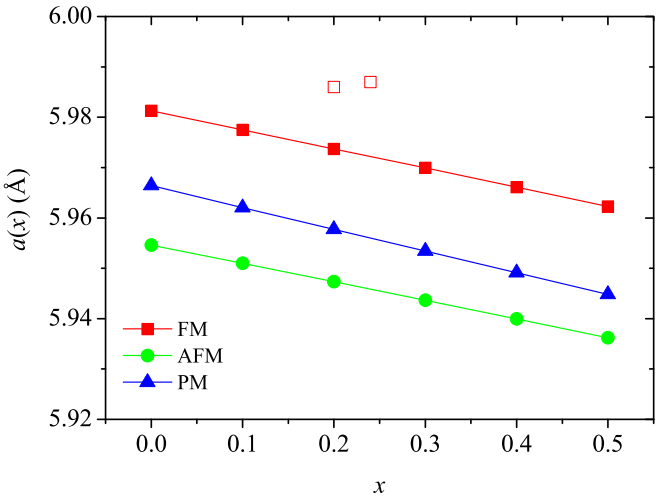

FIG. 2. (Color online) Composition (x) dependence of the equilibrium lattice parameter $a(x)$ of the $L2_1$-$Ni_{2-x}Co_xMn_{1.60}Sn_{0.40}$ ($0 \leqslant x \leqslant 0.50$) with FM, AFM, and PM states, respectively. The solid points denote our present $a(x)$ values. The open squares mean the experimental $a(x)$ for $x = 0.20$ and 0.24, which are from Refs. [20] and [15], respectively.

shown against x. In any of the three magnetic states, the $a(x)$ decreases linearly with increasing x. In each composition, the $a(x)$ is always biggest in the FM state but smallest in the AFM one. The open squares in the figure denote the experimental data for $x = 0.20$ and 0.24, respectively [15,20]. It is clear that our present $a(x)$ in the FM sate is in much better agreement with them than those in the AFM and PM states. Since these experimental $a(x)$ are measured above room temperature [15,20], they are shown a little larger than our values in the FM state due to the thermal expansion.

The x dependences of the lattice parameters [$a(x)$ and $c/a(x)$] of the tetragonal martensite are depicted in Fig. 3. With increasing x, the $a(x)$ in both the AFM and PM states decrease linearly as well. Nevertheless, the $c/a(x)$ decreases in the AFM state but keeps almost constant around 1.20 in the PM state. It is noted that in the AFM state the $c/a(x)$ values are around 1.25–1.31, which are comparable to the data (1.31) calculated in $Ni_2Mn_{1.50}Sn_{0.50}$ [38]. In addition, following the relationship of $T_M(x) \sim c/a(x)$ found in the NiMn-based alloys [39,40], a larger $c/a(x)$ corresponds to a higher $T_M(x)$; the present decrease of $c/a(x)$ in the AFM state happens to correspond to the decrease of the experimental $T_M(x)$ with Co addition in $Ni_{2-x}Co_xMn_{1.60}Sn_{0.40}$ [15,20,41].

B. Elastic property

In Table II, the calculated bulk modulus $B(x)$, elastic constants $C_{ij}(x)$, and Debye temperature $\Theta(x)$ of the FM, AFM, and PM $L2_1$-$Ni_{2-x}Co_xMn_{1.60}Sn_{0.40}$ ($0 \leqslant x \leqslant 0.50$) alloys are listed. According to the dynamical or mechanical stability condition of a lattice, the stability criteria for cubic crystals requires that $C_{11} > |C_{12}|$, $C_{11} + 2C_{12} > 0$, and $C_{44} > 0$. From our calculations, these $C_{ij}(x)$ of the FM and PM states satisfy all of the above conditions. However, in the AFM state, the $C_{11}(x)$ is smaller than $|C_{12}(x)|$ when

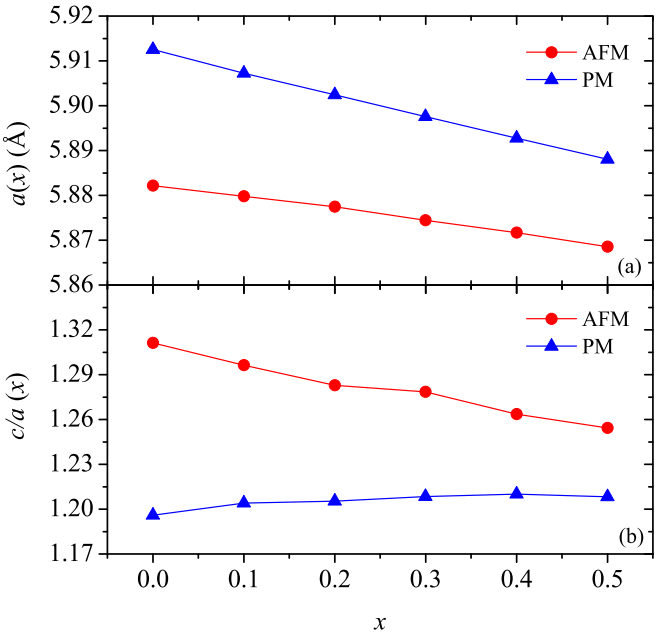

FIG. 3. (Color online) Composition (x) dependence of the equilibrium lattice parameters [$a(x)$ in (a) and $c/a(x)$ in (b)] of the tetragonal $Ni_{2-x}Co_xMn_{1.60}Sn_{0.40}$ ($0 \leqslant x \leqslant 0.50$) with AFM and PM states, respectively.

$0 \leqslant x \leqslant 0.40$, and for $x = 0.50$ they are almost comparable because $C'(x)\{=\frac{1}{2}[C_{11}(x) - C_{12}(x)]\}$ is merely about 0.9 GPa in this composition. It is supposed that the $C_{ij}(x)$ in the AFM state do not follow the requirement of $C_{11}(x) > |C_{12}(x)|$. Neglecting the temperature effect on the $C_{ij}(x)$, the AFM $L2_1$-$Ni_{2-x}Co_xMn_{1.60}Sn_{0.40}$ therefore is mechanically unstable in low temperature. This may be the reason why $Ni_2Mn_{1.60}Sn_{0.40}$ is measured with the FM state but not the AFM one at 4.2 K [41,42], in spite of the latter one being confirmed energetically favorable from above calculations. In the present work, all these studied austenitic alloys are confirmed both thermodynamically and mechanically stabilized by the FM state at 0 K, which is in good agreement with the experimental measurements in low temperatures [7,43].

TABLE II. Composition (x) dependence of the theoretical bulk modulus [$B(x)$, in GPa], elastic constants [$C_{ij}(x)$, in GPa], and Debye temperature [$\Theta(x)$, in K] of the FM, AFM, and PM $L2_1$-$Ni_{2-x}Co_xMn_{1.60}Sn_{0.40}$ ($0 \leqslant x \leqslant 0.50$). The tetragonal shear elastic constant $C'(x) = \frac{1}{2}[C_{11}(x) - C_{12}(x)]$.

States	x	$B(x)$	$C_{11}(x)$	$C_{12}(x)$	$C_{44}(x)$	$C'(x)$	$\Theta(x)$
FM	0.00	144.6	160.6	136.6	114.8	12.0	332.2
	0.10	145.8	163.5	136.9	116.2	13.3	340.9
	0.20	147.0	167.1	136.9	117.7	15.1	350.8
	0.30	148.2	171.0	136.8	119.2	17.1	361.7
	0.40	149.4	175.5	136.3	120.4	19.6	373.5
	0.50	150.8	180.4	136.0	122.2	22.2	385.1
AFM	0.00	143.2	141.5	144.1	122.7	−1.3	
	0.10	143.9	141.6	145.0	124.2	−1.7	
	0.20	144.7	142.4	145.8	125.7	−1.7	
	0.30	145.5	143.9	146.3	127.3	−1.2	
	0.40	146.3	145.9	146.5	128.7	−0.3	
	0.50	147.2	148.4	146.6	130.3	0.9	
PM	0.00	142.4	152.4	137.4	119.3	7.5	300.9
	0.10	143.4	151.4	139.4	120.6	6.0	286.4
	0.20	144.3	151.0	141.0	121.9	5.0	274.3
	0.30	145.3	151.0	142.4	123.1	4.3	265.2
	0.40	146.4	151.6	143.8	124.5	3.9	259.8
	0.50	147.5	152.4	145.0	125.8	3.7	257.1

In Table III, the calculated $B(x)$, $C_{ij}(x)$, and $\Theta(x)$ in the AFM and PM martensite are listed. The dynamical or mechanical stability criteria for tetragonal crystals requires that $C_{11} > |C_{12}|$, $C_{33} > 0$, $C_{44} > 0$, $C_{66} > 0$, $(C_{11} + C_{33} - 2C_{13}) > 0$, and $(2C_{11} + C_{33} + 2C_{12} + 4C_{13}) > 0$. Our present $C_{ij}(x)$ in both the AFM and PM states follow these conditions. Since the AFM martensite is relatively lower in energy than the PM one, the martensite of all these alloys is both thermodynamically and mechanically stabilized by the AFM ordering between Mn_1 and Mn_2 at 0 K. The antiparallel alignment between Mn_1 and Mn_2 has been confirmed in the tetragonal structure of $Ni_2Mn_{1+x}Sn_{1-x}$ ternary alloys by means of both first-principle calculations [38,44] and neutron-diffraction experiment [45]. Although around room temperature, several different magnetic states have been reported in the martensitic NiCoMnSn quaternary alloys [7,12,14,20,43], such as antiferromagneticlike, ferrimagnetic, paramagnetic, superparamagnetic, and superspin-glass states. Almost all of these nonferromagnetic states indicate the existence of the AFM coupling between Mn_1 and Mn_2 in the phase. Therefore, in the present work it is seen as reasonable that with less than 25% Ni replaced with Co in $Ni_{2-x}Co_xMn_{1.60}Sn_{0.40}$ the martensite still remains in the AFM state at 0 K.

In Tables II and III, the tetragonal shear elastic modulus of the austenite, $C'(x)$, and that of the martensite $\{C_s(x)[= C_{11}(x) + C_{12}(x) + 2C_{33}(x) - 4C_{13}(x)]\}$ are especially shown for comparison. It is found that in the same composition x the $C'(x)$ is very small whereas the $C_s(x)$ is relatively quite large. The particularly low value of $C'(x)$ indicates a strong negative contribution of the entropy ($-TS$) to the free energy (F) of the austenite, which ultimately stabilizes the phase against the martensite with increasing T. The FM and AFM couplings between the Mn_1 and Mn_2 in $Ni_{2-x}Co_xMn_{1.60}Sn_{0.40}$ correspond to the ground-state magnetic ordering of the austenite and martensite, respectively. With increasing x (or decreasing e/a), the $C'(x)$ in the FM state increases whereas the $C_s(x)$ in the AFM state decreases. The Co doping tends to mechanically stabilize the cubic relative to the tetragonal structure in low temperature, which results in lower experimental $T_M(x)$ of this type of alloys [15,20,41].

In the PM state, the $C'(x)$ decreases but the $C_s(x)$ increases with increasing x (or decreasing e/a), preferring the stability of the martensite relative to the austenite. Then, the opposite trend of experimental $T_M(x) \sim x$ is estimated. It means that the 0-K $C'(x) \sim x$ and $C_s(x) \sim x$ in the PM state fail to account for the experimental trend of $T_M(x) \sim x$. This failure could be ascribed to the fact that, in the high-temperature PM state, the temperature effects on the elastic constants, such as electronic entropy, phonon smearing, thermal expansion, and magnetism [46], might be significant and thus could not be ignored.

TABLE III. Composition (x) dependence of the theoretical bulk modulus [$B(x)$, in GPa], elastic constants [$C_{ij}(x)$, in GPa], and Debye temperature [$\Theta(x)$, in K] of the AFM and PM tetragonal $Ni_{2-x}Co_xMn_{1.60}Sn_{0.40}$ ($0 \leqslant x \leqslant 0.50$). The tetragonal shear elastic constant $C_s(x) = C_{11}(x) + C_{12}(x) + 2C_{33}(x) - 4C_{13}(x)$.

States	x	$B(x)$	$C_{11}(x)$	$C_{12}(x)$	$C_{13}(x)$	$C_{33}(x)$	$C_{44}(x)$	$C_{66}(x)$	$C_s(x)$	$\Theta(x)$
AFM	0.00	145.8	177.5	118.3	128.8	188.2	99.9	88.1	157.0	377.7
	0.10	146.4	182.3	114.7	129.6	188.4	104.4	89.4	155.4	385.7
	0.20	147.0	184.5	113.7	130.2	189.1	108.8	90.9	155.7	389.9
	0.30	147.8	189.5	109.7	133.4	183.8	110.8	92.5	133.0	388.7
	0.40	148.5	195.0	105.6	134.0	184.8	116.0	93.1	134.2	396.4
	0.50	149.3	199.1	102.9	135.7	183.3	119.9	94.0	125.6	398.1
PM	0.00	141.4	198.6	86.0	134.1	159.6	117.9	58.9	67.3	356.0
	0.10	142.6	197.9	89.5	134.0	164.1	117.6	65.1	79.4	365.7
	0.20	144.0	199.8	90.6	134.2	168.4	122.1	69.3	90.3	377.0
	0.30	145.3	201.0	92.2	134.8	171.4	119.9	73.9	96.7	388.1
	0.40	146.6	202.6	93.2	135.9	173.4	121.0	77.4	99.2	383.7
	0.50	147.9	205.3	93.3	137.0	175.2	122.8	79.7	101.1	388.0

C. Phase stability

In NiMn-based shape-memory alloys [47,48], the large free-energy difference between the austenite and martensite (ΔF^{AM}) generally means the big driving force of the MPT, and then the high critical temperature T_M. Here, we calculate the $\Delta F^{\mathrm{AM}}(x)$ with the approximation, $\Delta F^{\mathrm{AM}}(x) \approx \Delta E^{\mathrm{AM}}(x) + \Delta F^{\mathrm{AM}}_{\mathrm{ph}}(x)$, where the $\Delta E^{\mathrm{AM}}(x)$ is the electronic energy difference between the austenite and martensite and the $\Delta F^{\mathrm{AM}}_{\mathrm{ph}}(x)$ is that of the phonon vibrational free-energy difference. The $\Delta F^{\mathrm{AM}}_{\mathrm{ph}}(x)$ may be calculated with Eq. (5) in a previous paper [49], which is nevertheless very time consuming because of the temperature-dependent Debye temperature term [46]. For the sake of simplicity, the present 0-K $\Delta F^{\mathrm{AM}}_{\mathrm{ph}}(x)$ is evaluated from its zero-point expression, $\Delta F^{\mathrm{AM}}_{\mathrm{ph}}(x) \approx \frac{9}{8}k_B[\Theta^A(x) - \Theta^M(x)]$, with the $\Theta^A(x)$ and $\Theta^M(x)$ being the Debye temperature in the austenite and martensite, respectively [30]. In finite temperature, the $\Delta F^{\mathrm{AM}}_{\mathrm{ph}}(x)$ is simply estimated from its high-temperature expansion, $\Delta F^{\mathrm{AM}}_{\mathrm{ph}}(x) \approx 3k_BT\frac{\Theta^A(x)-\Theta^M(x)}{\Theta^A(x)}$ [50]. Listed in Tables II and III, in addition to the fact that the $C'(x)$ is much smaller than the $C_s(x)$, the $\Theta^A(x)$ is always smaller than $\Theta^M(x)$ in each x. This means that the $\Delta F^{\mathrm{AM}}_{\mathrm{ph}}(x)$ provides a negative contribution to the $\Delta F^{\mathrm{AM}}(x)$.

With the obtained ground-state magnetic ordering of the two phases, we calculate the $\Delta F^{\mathrm{AM}}(x)$ of $Ni_{2-x}Co_xMn_{1.60}Sn_{0.40}$ ($0 \leqslant x \leqslant 0.50$) in different temperatures from 0 to 500 K with intervals of 100 K. In Fig. 4, the estimated $\Delta F^{\mathrm{AM}}(x) \sim x$ is shown in each temperature, in comparison with the available experimental $T_M(x) \sim x$. It is clear that in each x the $\Delta F^{\mathrm{AM}}(x)$ indeed decreases with increasing T because of the negative contribution of the $\Delta F^{\mathrm{AM}}_{\mathrm{ph}}(x)$, which prefers the relative stability of the parent phase. With increasing x (or decreasing e/a), the $\Delta F^{\mathrm{AM}}(x)$ decreases in each temperature, corresponding to the $T_M(x)$ decreasing with the Co doping [15,20,41].

Positive $\Delta F^{\mathrm{AM}}(x)$ means that the AFM martensite is lower in energy and then more stable than the FM austenite, whereas negative $\Delta F^{\mathrm{AM}}(x)$ means that the latter one is more stable. In Fig. 4, the 0-K $\Delta F^{\mathrm{AM}}(x)$ is close to zero around $x = 0.43$, reflecting that the austenite and martensite of the alloy are energetically comparable at 0 K. For alloys with $x < 0.43$, the AFM martensite is relative more stable in low temperature because $\Delta F^{\mathrm{AM}}(x)$ tends to be positive, whereas above $x = 0.43$ due to $\Delta F^{\mathrm{AM}}(x) < 0$ the FM austenite is always stabilized at ambient temperature. It suggests that even in very low temperature the alloys with $x > 0.43$ would not undergo MPT and instead they are stabilized with the FM cubic structure. The predicted critical composition ($x = 0.43$) of whether the MPT can occur or not in $Ni_{2-x}Co_xMn_{1.60}Sn_{0.40}$ is comparable to that (around 0.32–0.36) measured in $Ni_{2-x}Co_xMn_{1.56}Sn_{0.44}$ [12].

D. Magnetic property

In Table IV, the 0-K local magnetic moments of Ni, Co, two types of Mn, and Sn atoms, together with the total magnetic moments of $Ni_{2-x}Co_xMn_{1.60}Sn_{0.40}$ alloys are summarized.

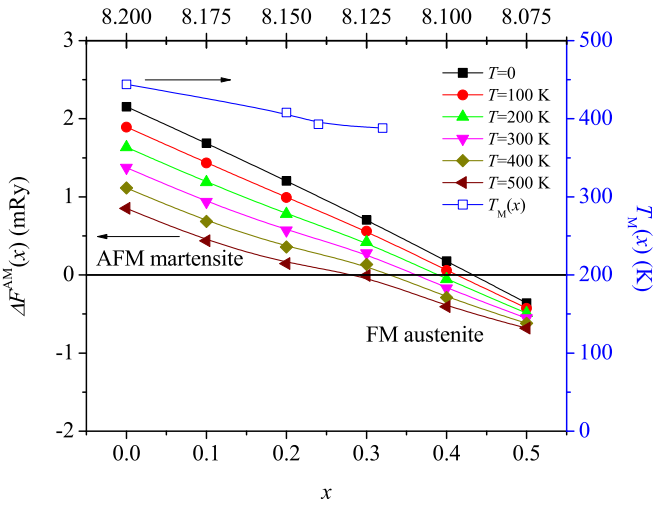

FIG. 4. (Color online) Free-energy difference between the FM austenite and the AFM martensite [$\Delta F^{\mathrm{AM}}(x)$], together with the available experimental $T_M(x)$ of $Ni_{2-x}Co_xMn_{1.60}Sn_{0.40}$ ($0 \leqslant x \leqslant 0.50$) with respect to x and the number of valence electrons per atom (e/a). The $\Delta F^{\mathrm{AM}}(x)$ is calculated in different temperatures from 0 to 500 K with intervals of 100 K. The $T_M(x)$ are cited from Refs. [15,20,41].

TABLE IV. Local magnetic moments (in μ_B) of Ni, Co, and Mn on Mn(Mn_1) and Sn sites (Mn_2), and Sn atoms, together with the total magnetic moments (in μ_B) of the FM, AFM, and PM states of $Ni_{2-x}Co_xMn_{1.60}Sn_{0.40}$ ($0 \leqslant x \leqslant 0.50$).

States	Ni	Co	Mn_1	Mn_2	Sn	Tot
FM	0.55	1.34	3.48	3.49	−0.05	6.70–6.98
AFM	0.13	0.65	3.40	−3.45	−0.05	1.55–1.77
PM	0	0	3.44(−3.44)	3.45(−3.45)	0	0

The concentration of Co as well as the crystal structure do not influence these local magnetic moments significantly, and therefore, in the table we show them only as a function of the magnetic ordering for the alloy with $x = 0.1$. It is found that, in all the FM, AFM, and PM states, the Mn_1 and Mn_2 atoms are spin polarized, and in absolute value their magnetic moments (around 3.45 μ_B) are almost the same. The Ni and Co atoms are spin polarized only in the FM and AFM states. Their magnetic moments are always parallel to those of the Mn atoms on the Mn sublattice, and the values in the AFM state (0.13 μ_B for Ni, 0.65 μ_B for Co) turn out to be lower than their correspondents in the FM one (0.55 μ_B for Ni, 1.34 μ_B for Co). The Sn atoms are almost non-spin-polarized in all the three magnetic states. In a result, the 0-K total magnetic moment is around 6.70 $\mu_B \sim 6.98\,\mu_B$ in the FM state, and 1.55 $\mu_B \sim 1.77\,\mu_B$ in the AFM state. It reveals that with x increasing from 0 to 0.50 the total magnetic moments show an increase of less than 0.30 μ_B in both the FM and AFM states of alloys.

In order to explore the magnetic transition from the FM state to the PM one of the austenitic alloys in finite temperature, we calculate both the M and χ of these alloys at different temperatures from 0 to 700 K with intervals of 25 K, by means of EMTO-CPA in combination with UppASD method. In Fig. 5, the obtained temperature dependence of the χ as well as the normalized magnetization (M/M_0, with M and M_0 being the magnetization at T and 0 K, respectively) are shown for each x, together with the $T_C(x)$ estimated from the temperature corresponding to the maximum of χ. It is found that with increasing x from 0 to 0.50 our theoretical $T_C(x)$ monotonically goes up from 317 to 424 K, which is in line with the available experimental data [$T_C^{\mathrm{Exp.}}(x)$] [15,20,41] shown in Fig. 6. Similar to Fe-doped NiMn-based alloys [51], the Co addition increases the $T_C(x)$ and then enhances the saturated magnetization under the magnetic field, which is consequently hoped to improve the output stress of these alloys during the MPT.

Seen from the energy calculations in Fig. 6, it is shown that the electronic energy difference between the PM and the FM austenite [$\Delta E_{\mathrm{PF}}(x)$] linearly increases with x, which is consistent with the trend of $T_C(x) \sim x$. It indicates that the relationship of $T_C(x) \sim x$ should be originated from the trend of $\Delta E_{\mathrm{PF}}(x) \sim x$, i.e., the Co addition increases the magnetic

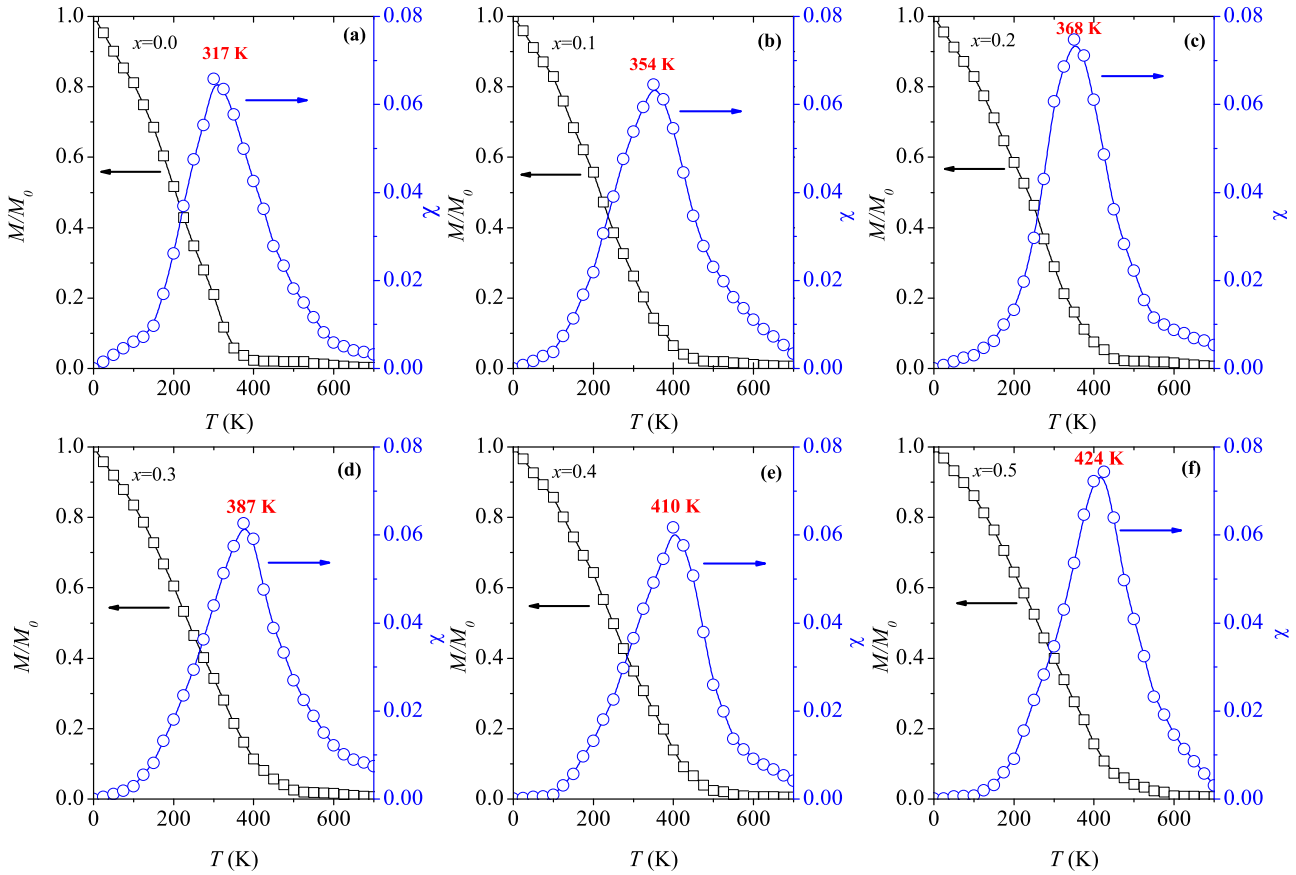

FIG. 5. (Color online) Normalized magnetic moment (M/M_0, with M and M_0 being the magnetization at T and 0 K, respectively) as well as susceptibility (χ) with respect to temperature (T), together with the estimated $T_C(x)$ of $Ni_{2-x}Co_xMn_{1.60}Sn_{0.40}$ ($0 \leqslant x \leqslant 0.50$).

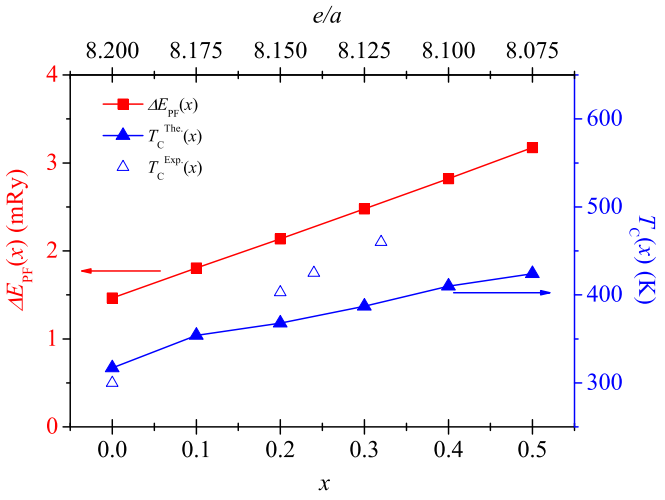

FIG. 6. (Color online) Total electronic energy difference between the PM and FM austenite [$\Delta E_{PF}(x)$] as well as the $T_C(x)$ of $L2_1$-$Ni_{2-x}Co_xMn_{1.60}Sn_{0.40}$ ($0 \leqslant x \leqslant 0.50$) with respect to x and the number of valence electrons per atom (e/a). The $T_C^{the}(x)$ denotes the present theoretical values whereas the $T_C^{exp.}(x)$ means the experimental data from Refs. [15,20,41].

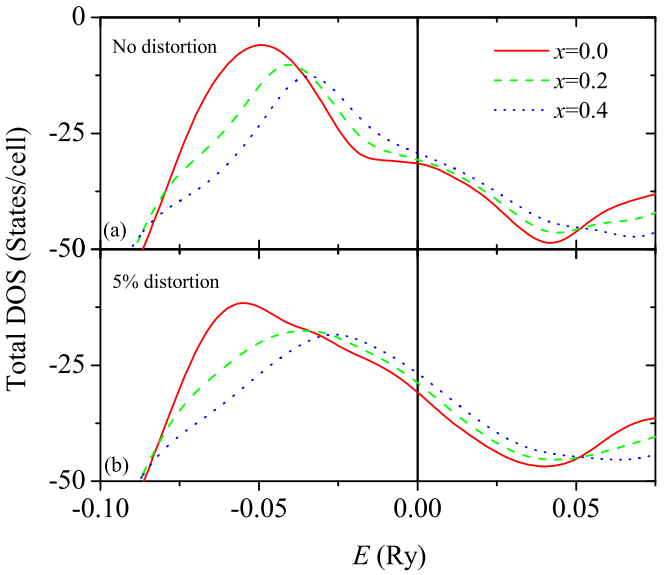

FIG. 7. (Color online) Total minority (spin-down) density of states (DOS) of FM $L2_1$-$Ni_{2-x}Co_xMn_{1.60}Sn_{0.40}$ ($x = 0$, 0.20, and 0.40) with no lattice distortion (a) and 5% tetragonal distortion used to calculate $C'(x)$ (b). The vertical lines indicate the Fermi level.

excitation energy and therefore enhances the driving force of the magnetic transition from the FM state to the PM one in $Ni_{2-x}Co_xMn_{1.60}Sn_{0.40}$.

E. Electronic structure

The stability of the parent phase in NiMn-based alloys has been demonstrated to be closely related to the minority (spin-down) density of states (DOS) around Fermi level [52–54]. In order to explore the electronic origin of the composition-dependent MPT, we calculate and compare the DOS of FM $L2_1$-$Ni_{2-x}Co_xMn_{1.60}Sn_{0.40}$ ($x = 0$, 0.20, and 0.40) alloys with 0 and 5% tetragonal distortion used to calculate $C'(x)$, as shown in Fig. 7. For $Ni_2Mn_{1.60}Sn_{0.40}$, there exits a pseudogap in the total DOS both with and without lattice distortion at about -0.05 Ry, which was shown to be the covalent bonding characters between Sn p and Ni $3d$ as well as Co $3d$ electrons [55]. However, for the total DOS without lattice distortion [in Fig. 7(a)], a small peak appears at about -0.02 Ry below the Fermi level, resulting in the Jahn-Teller instability of the cubic phase [52,54,56–58] of $Ni_2Mn_{1.60}Sn_{0.40}$. Upon tetragonal distortion [in Fig. 7(b)], this peak splits and then the DOS near the Fermi level reduces, leading to a more stable tetragonal phase of the alloy.

Shown in Fig. 7, with increasing x the pseudogap is gradually filled and then becomes more and more shallow. It deserves to be noted that with Co doping [in Fig. 7(a)] the small peak gradually disappears. Upon 5% tetragonal distortion [in Fig. 7(b)], its splitting is thus less and less significant with increasing x. This means that the Co doping reduces the Jahn-Teller instability and then depresses the tetragonal lattice distortion, which corresponds to the increase of $C'(x)$ but the decrease of the $T_M(x)$ with the Co addition.

In comparison to the DOS of Ni as well as Co atoms shown in Fig. 8, it is found that the pseudogap is formed by the Ni $3d$ and Co $3d$ states. Both of them include triple-degenerated T_{2g} and double-degenerated E_g bands. In Figs. 8(a) and 8(c), the pseudogap formed by Ni $3d$ T_{2g} and Ni $3d$ E_g is around -0.05 Ry. In Figs. 8(b) and 8(d), the pseudogap formed by Co $3d$ T_{2g} and Co $3d$ E_g is in a relative higher energy level, which is almost right on the Fermi level. Therefore, with Ni replacing with Co, the hybridization between Ni $3d$ and Co $3d$ electrons around -0.05 Ry becomes more and more strong, and the pseudogap in the place is gradually filled for $Ni_{2-x}Co_xMn_{1.60}Sn_{0.40}$.

In Figs. 8(a) and 8(b), the small peak in the total DOS of $Ni_2Mn_{1.60}Sn_{0.40}$ is shown to be mainly contributed by Ni $3d$ E_g, whereas the Ni $3d$ T_{2g} as well as the whole Co $3d$ states seem to have no connection with the peak. In Fig. 8(c), upon 5% tetragonal distortion, the Ni $3d$ E_g of the alloy splits into two levels: one is on a little higher energy side with the $x^2 - y^2$ orbital, whereas the other one is on the relative lower energy side with the $3z^2 - r^2$ orbital. With increasing x, the Ni $3d$ E_g states reduce and the peak is weakened [in Fig. 8(a)]. Upon tetragonal distortion [in Fig. 8(c)], its splitting is therefore less and less with the Co addition, meaning that the Jahn-Teller instability in the total DOS reduces and the FM cubic structure gets relatively more and more stable with increasing x in $Ni_{2-x}Co_xMn_{1.60}Sn_{0.40}$.

IV. CONCLUSION

Using first-principles EMTO-CPA in combination with UppASD method, we have systematically investigated the composition-dependent crystal structure, lattice parameters, elastic property, phase stability, Curie temperature, and electronic structure of $Ni_{2-x}Co_xMn_{1.60}Sn_{0.40}$ ($0 \leqslant x \leqslant 0.50$) quaternary shape-memory alloys. The main results are summarized as follows.

(1) The present lattice parameters $a(x)$ and $c/a(x)$ of the FM austenite and the AFM martensite decrease with increasing

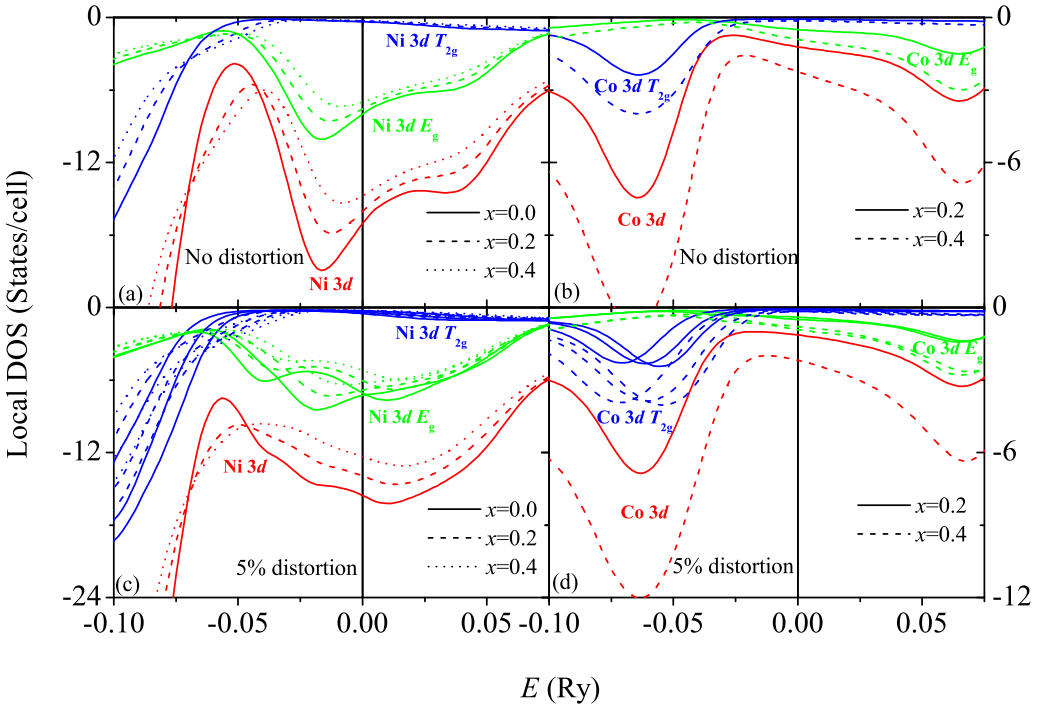

FIG. 8. (Color online) Minority (spin-down) density of states (DOS) of Ni 3d, Ni 3d E_g, and Ni 3d T_{2g} as well as Co 3d, Co 3d E_g, and Co 3d T_{2g} in FM $L2_1$-$Ni_{2-x}Co_xMn_{1.60}Sn_{0.40}$ ($x = 0$, 0.20, and 0.40) with no lattice distortion (upper panel) and 5% tetragonal distortion used to calculate $C'(x)$ (lower panel). The figure illustrates how T_{2g} and E_g bands of Ni 3d as well as Co 3d are split by the lattice distortion. The vertical lines indicate the Fermi level.

x, which are in good agreement with the available theoretical and experimental data.

(2) The MPT is found occurring below $x = 0.43$. Above the composition, the alloys are stabilized by the FM cubic $L2_1$ phase even in very low temperature. For $x < 0.43$, the austenite is stabilized by the FM coupling between Mn_1 and Mn_2, whereas the martensite is with the AFM ordering at 0 K.

(3) With increasing x (or decreasing e/a), the $c/a(x)$ of the AFM martensite decreases, the shear elastic modulus of the FM austenite $C'(x)$ increases whereas that of the AFM martensite $C_s(x)$ decreases, and the free-energy difference between the two phases $\Delta F^{\mathrm{AM}}(x)$ decreases, which all well account for the decrease of the experimental $T_M(x)$ with increasing x.

(4) The estimated $T_C(x) \sim x$ is in line with the available experimental data. With the Co addition, the magnetic excitation energy $\Delta E_{\mathrm{PF}}(x)$ increases, which therefore enhances the driving force of the magnetic transition from the FM state to the PM one.

(5) The calculated electronic structure indicates that the Ni 3d as well as the Co 3d states near the Fermi level mainly dominate the phase stability of these studied alloys.

ACKNOWLEDGMENTS

The authors acknowledge financial support from the National Natural Science Foundation of China under Grants No. 51171187, No. 51271181, and No. 51301176 and the Ministry of Science and Technology of China under Grant No. 2014CB644001. The China Postdoctoral Science Foundation is acknowledged for financial support. C.-M.L. is also grateful to the T. S. Kê Research Fellowship of the Institute of Metal Research, Chinese Academy of Sciences, in cooperation with Shenyang National Laboratory for Material Science.

[1] R. Kainuma, Y. Imano, W. Ito, Y. Sutou, H. Morito, S. Okamoto, O. Kitakami, K. Oikawa, A. Fujita, T. Kanomata, and K. Ishida, Nature (London) **439**, 957 (2006).

[2] H. E. Karaca, I. Karaman, B. Basaran, Y. Ren, Y. I. Chumlyakov, and H. J. Maier, Adv. Funct. Mater. **19**, 983 (2009).

[3] W. Zhu, E. K. Liu, L. Feng, X. D. Tang, J. L. Chen, G. H. Wu, H. Y. Liu, F. B. Meng, and H. Z. Luo, Appl. Phys. Lett. **95**, 222512 (2009).

[4] U. Gaitzsch, M. Pötschke, S. Roth, B. Rellinghaus, and L. Schultz, Acta Mater. **57**, 365 (2009).

[5] A. Sozinov, A. A. Likhachev, N. Lanska, and K. Ullakko, Appl. Phys. Lett. **80**, 1746 (2002).

[6] K. Ullakko, J. K. Huang, C. Kantner, R. C. O'Handley, and V. V. Kokorin, Appl. Phys. Lett. **69**, 1966 (1996).

[7] R. Kainuma, Y. Imano, W. Ito, H. Morito, Y. Sutou, K. Oikawa, A. Fujita, K. Ishida, S. Okamoto, O. Kitakami, and T. Kanomata, Appl. Phys. Lett. **88**, 192513 (2006).

[8] C. Jing, Z. Li, H. L. Zhang, J. P. Chen, Y. F. Qiao, S. X. Cao, and J. C. Zhang, Eur. Phys. J. B **67**, 193 (2009).

[9] H. S. Liu, C. L. Zhang, Z. D. Han, H. C. Xuan, D. H. Wang, and Y. W. Du, J. Alloys Compd. **467**, 27 (2009).

[10] J. Marcos, L. Mañosa, A. Planes, F. Casanova, X. Batlle, and A. Labarta, Phys. Rev. B **68**, 094401 (2003).

[11] V. D. Buchelnikov, V. V. Sokolovskiy, H. C. Herper, H. Ebert, M. E. Gruner, S. V. Taskaev, V. V. Khovaylo, A. Hucht, A. Dannenberg, M. Ogura, H. Akai, M. Acet, and P. Entel, Phys. Rev. B **81**, 094411 (2010).

[12] D. Y. Cong, S. Roth, M. Potschke, C. Hurrich, and L. Schultz, Appl. Phys. Lett. **97**, 021908 (2010).

[13] F. Chen, Y. X. Tong, B. Tian, Y. F. Zheng, and Y. Liu, Intermetallics **18**, 188 (2010).

[14] F. Chen, Y. X. Tong, Y. J. Huang, B. Tian, L. Li, and Y. F. Zheng, Intermetallics **36**, 81 (2013).

[15] K. P. Bhatti, S. El-Khatib, V. Srivastava, R. D. James, and C. Leighton, Phys. Rev. B **85**, 134450 (2012).

[16] K. Ito, W. Ito, R. Y. Umetsu, S. Tajima, H. Kawaura, R. Kainuma, and K. Ishida, Scr. Mater. **61**, 504 (2009).

[17] F. Chen, Y. X. Tong, X. L. Lu, B. Tian, L. Li, and Y. F. Zheng, J. Mater. Eng. Perform. **21**, 2509 (2012).

[18] D. Y. Cong, S. Roth, J. Liu, Q. Luo, and M. Pötschek, Appl. Phys. Lett. **96**, 112504 (2010).

[19] R. Y. Umetsu, K. Ito, W. Ito, K. Koyama, T. Kanomata, K. Ishida, and R. Kainuma, J. Alloys Compd. **509**, 1389 (2011).

[20] V. Srivastava, X. Chen, and R. D. James, Appl. Phys. Lett. **97**, 014101 (2010).

[21] C. Biswas, R. Rawat, and S. R. Barman, Appl. Phys. Lett. **86**, 202508 (2005).

[22] C. M. Li, H. B. Luo, Q. M. Hu, R. Yang, B. Johansson, and L. Vitos, Phys. Rev. B **82**, 024201 (2010).

[23] L. Vitos, Phys. Rev. B **64**, 014107 (2001).

[24] L. Vitos, *Computational Quantum Mechanics for Materials Engineers* (Springer-Verlag, London, 2007).

[25] O. K. Andersen, O. Jepsen, and G. Krier, in *Lectures on Methods of Electronic Structure Calculations*, edited by V. Kumar, O. K. Andersen, and A. Mookerjee (World Scientific, Singapore, 1994), pp. 63–124.

[26] J. Kollár, L. Vitos, and H. L. Skriver, in *Electronic Structure and Physical Properties of Solids: The Uses of the LMTO Method*, Lectures Notes in Physics, edited by H. Dreyssé (Springer-Verlag, Berlin, 2000), p. 85.

[27] L. Vitos, I. A. Abrikosov, and B. Johansson, Phys. Rev. Lett. **87**, 156401 (2001).

[28] B. L. Györffy, Phys. Rev. B **5**, 2382 (1972).

[29] V. L. Moruzzi, J. F. Janak, and K. Schwarz, Phys. Rev. B **37**, 790 (1988).

[30] C. M. Li, Q. M. Hu, R. Yang, B. Johansson, and L. Vitos, Phys. Rev. B **82**, 094201 (2010).

[31] R. Hill, Phys. Soc. A **65**, 349 (1952); J. Mech. Phys. Solids **11**, 357 (1963).

[32] J. Staunton, B. L. Györffy, A. J. Pindor, G. M. Stocks, and H. Winter, J. Magn. Magn. Mater. **45**, 15 (1984).

[33] B. Skubic, J. Hellsvik, L. Nordström, and O. Eriksson, J. Phys. Condens. Matter **20**, 315203 (2008).

[34] V. P. Antropov, M. I. Katsnelson, B. N. Harmon, M. van Schilfgaarde, and D. Kusnezov, Phys. Rev. B **54**, 1019 (1996).

[35] J. L. García-Palacios and F. J. Lázaro, Phys. Rev. B **55**, 1006 (1997).

[36] R. E. Watson, M. Blume, and G. H. Vineyard, Phys. Rev. **181**, 811 (1969).

[37] A. Liechtenstein, M. I. Katsnelson, and V. A. Gubanov, J. Phys. F **14**, L125 (1984); A. Liechtenstein, M. I. Katsnelson, V. P. Antropov, and V. A. Gubanov, J. Magn. Magn. Mater. **67**, 65 (1987).

[38] M. Ye, A. Kimura, Y. Miura, M. Shirai, Y. T. Cui, K. Shimada, H. Namatame, M. Taniguchi, S. Ueda, K. Kobayashi, R. Kainuma, T. Shishido, K. Fukushima, and T. Kanomata, Phys. Rev. Lett. **104**, 176401 (2010).

[39] N. Lanska, O. Söderberg, A. Sozinov, Y. Ge, K. Ullakko, and V. K. Lindroos, J. Appl. Phys. **95**, 8074 (2004).

[40] S. Banik, R. Ranjan, A. Chakrabarti, S. Bhardwaj, N. P. Lalla, A. M. Awasthi, V. Sathe, D. M. Phase, P. K. Mukhopadhyay, D. Pandey, and S. R. Barman, Phys. Rev. B **75**, 104107 (2007).

[41] T. Krenke, M. Acet, E. F. Wassermann, X. Moya, L. Mañosa, and A. Planes, Phys. Rev. B **72**, 014412 (2005).

[42] W. Ito, X. Xu, R. Y. Umetsu, T. Kanomata, and K. Ishida, Appl. Phys. Lett. **97**, 242512 (2010).

[43] D. Y. Cong, S. Roth, and L. Schultz, Acta Mater. **60**, 5335 (2012).

[44] V. V. Sokolovskiy, V. D. Buchelnikov, M. A. Zagrebin, P. Entel, S. Sahoo, and M. Ogura, Phys. Rev. B **86**, 134418 (2012).

[45] S. Aksoy, M. Acet, P. P. Deen, L. Mañosa, and A. Planes, Phys. Rev. B **79**, 212401 (2009).

[46] C. M. Li, H. B. Luo, Q. M. Hu, R. Yang, B. Johansson, and L. Vitos, Phys. Rev. B **84**, 174117 (2011).

[47] A. Chakrabarti, C. Biswas, S. Banik, R. S. Dhaka, A. K. Shukla, and S. R. Barman, Phys. Rev. B **72**, 073103 (2005).

[48] J. Chen, Y. Li, J. X. Shang, and H. B. Xu, Appl. Phys. Lett. **89**, 231921 (2006).

[49] P. Söderlind, L. Nordström, L. Yongming, and B. Johansson, Phys. Rev. B **42**, 4544 (1990).

[50] G. Grimvall, *Thermophysical Properties of Materials*, enlarged and revised ed. (North-Holland, Amsterdam, 1999).

[51] G. H. Wu, W. H. Wang, J. L. Chen, L. Ao, and Z. H. Liu, Appl. Phys. Lett. **80**, 634 (2002).

[52] C. P. Opeil, B. Mihaila, R. K. Schulze, L. Mañosa, A. Planes, W. L. Hults, R. A. Fisher, P. S. Riseborough, P. B. Littlewood, J. L. Smith, and J. C. Lashley, Phys. Rev. Lett. **100**, 165703 (2008).

[53] A. Ayuela, J. Enkovaara, and R. M. Nieminen, J. Phys. Condens. Matter **14**, 5325 (2002).

[54] P. Entel, V. D. Buchelnikov, V. V. Khovailo, A. T. Zayak, W. A. Adeagbo, M. E. Gruner, H. C. Herper, and E. Wassermann, J. Phys. D **39**, 865 (2006).

[55] C. M. Li, Q. M. Hu, R. Yang, B. Johansson, and L. Vitos, Phys. Rev. B **88**, 014109 (2013).

[56] P. J. Brown, A. Y. Bargawi, J. Crangle, K.-U. Neumann, and K. R. A. Ziebeck, J. Phys. Condens. Matter **11**, 4715 (1999).

[57] A. Ayuela, J. Enkovaara, K. Ullakko, and R. M. Nieminen, J. Phys. Condens. Matter **11**, 2017 (1999).

[58] V. V. Godlevsky and K. M. Rabe, Phys. Rev. B **63**, 134407 (2001).